© Indian Academy of Sciences

Influence of Mn_2O_3 on the physical properties of metallic glass network

P VINOTHKUMAR[1], M DHAVAMURTHY[2], MANOJ MOHAPATRA[3,4], A ANTONY SURESH[1] and PRIYA MURUGASEN[1,*]

[1]Department of Physics, Saveetha Engineering College, Thandalam, Chennai 602 105, India
[2]Department of Physics, St. Joseph's College of Engineering and Technology, Thanjavur 613403, India
[3]Radiochemistry Division, Bhabha Atomic Research Centre (BARC), Trombay, Mumbai 400 085, India
[4]HomiBhabha National Institute, Anushakti Nagar, Mumbai 400 094, India
*Corresponding author. E-mail: priyam7373@gmail.com

Abstract.   In this study, manganese ion was used as a dopant to improve the electrochemical characteristics of SrO_3–$BaCO_3$–B_2O_3, a manganese-based cathode material. Manganese-doped strontium barium borate (MSBB) glass was synthesized using the melt quenching procedure. UV–Vis spectroscopy was used to investigate linear optical characteristics such as optical band-gap energy (E_g), extinction coefficient (k), refractive index (n) and, optical and electrical conductivity. Furthermore, spectroscopy was employed to determine the existence of Mn^{2+} and Mn^{3+} oxidation states of manganese oxide in the glass composition. The dielectric characteristics (ε_r and tan δ) and ac conductivity (σ_{ac}) were examined at 30°C in the frequency range of 100 Hz to 5 MHz, and the space charge polarisation is dominant at the lower frequency domain, resulting in a high dielectric constant. The increase in frequency was accompanied by an increase in ac conductivity over shorter distances, which might be explained by the mobility carrier hopping process. The paramagnetic features of prepared glass at room temperature were confirmed by vibrating sample magnetometry (VSM). The electrochemical characteristics of the prepared glass electrode in a 6 M KOH electrolyte were investigated using cyclic voltammetry (CV), galvanostatic charge–discharge, and electrochemical impedance spectroscopy (EIS). The MSBB glass electrode has the highest specific capacitance of 84 F g^{-1} at 2 A g^{-1} and the highest power density of 1388 W kg^{-1}, with a specific energy density of 2 Wh kg^{-1}. The mechanical behavior of the prepared glass under various stresses was examined using Vickers hardness measurement. The mass attenuation coefficient (μ/ρ), the mean free path (MFP) and the half-value layer (HVL) of the prepared glass were all evaluated.

Keywords.   Optical conductivity; electrical conductivity; dielectric constant; hysteresis curve; cyclic voltammogram; specific capacitance.

PACS Nos.   78.66.Jg; 33.20.Lg; 62.20.Mk; 72.15.Cz

1. Introduction

Recent interest in research indicates that glass materials are being employed as electrolytes in electrochemical equipment including chemical sensors and batteries [1, 2]. Barium-based borate glasses are widely used in electronic, pharmaceutical, and industrial applications because of their superior refraction, low dispersion, strong electric resistance, low coefficient of thermal expansion, and low melting point [3, 4]. Glass modifiers like alkali and alkaline earth oxides can enable borate glasses to have enhanced physical and optical properties. Alkaline earth oxides (BaO, CaO, MgO and SrO) react with B_2O_3 to generate binary borate glasses with triangular and tetrahedral boron groups, as seen by infrared and Raman spectra [5, 6]. Alkaline earth oxide-based borate glasses have also been developed and are used in a variety of applications, including solar energy converters, vacuum ultraviolet optics, and radiation dosimetry. The addition of alkaline earth metals to the borate glass network causes favourable modifications, especially strontium (Sr^{2+}) functions as a good modifier. The doping of an appropriate amount of SrO into glass samples can significantly improve their

strength [7, 8]. According to Krogh Moe *et al* [9], an alkali oxide can convert a trigonal boron atom (BO_3) into a four-fold (BO_4) coordinated boron atom, by creating a bridging oxygen network between four oxygen and each BO_4 negatively charged structural group. The factors of conversion $BO_3 \rightarrow BO_4$ were associated with the increase in density, which was due to the introduction of strontium with a heavier atomic weight (87.62 amu). Furthermore, as the concentration of SrO increases, the increase in the boron–oxygen ratio could impact the increase in density [10]. SrO also enhances the stiffness of glass samples, which opens up new applications in biological systems and nonlinear optical devices [11].

When ionising radiation (γ-rays, X-rays, and high-energy electrons) is used to ionise a glass, the incident energy exceeds the band gap, causing electrons to be excited from the valence band. These electrons are transformed into kinetic energy and propelled into the glass, where they either recombine with positively charged holes to produce colour centers or become trapped within the glass to generate colour centers. The electrons are trapped or will recombine with holes when the electron energy is too low to ionise further electrons. A wide range of applications exists for glasses containing heavy metal oxides, including optical fibre amplifiers, energy storage devices, shielding window glass for radiation, and encapsulating radioactive wastes.

The energy density of conventional dielectric capacitors is lower, whereas secondary batteries offer a higher power density and longer life. As a result, it is essential to find the right electrode materials for supercapacitors. Electrochemical supercapacitors are employed in high-energy storage systems because of their advantages. In general, electrochemical supercapacitors were made using transition metal oxide glasses and polymers. Transition metal ions (Mn^{2+}, Ni^{2+}, Cr^{2+}, Fe^{3+}, etc.,) can perform as network formers or modifiers depending on their coordination number and redox state. Tetrahedral coordination is frequently related to network-forming properties and the octahedral bonding structure of cation modifies the network [11].

TM ions in the borate system of glasses are expected to enhance specific capacitance and capacity retention of electrochemical devices. Optical, dielectric, mechanical, and VSM studies have also been utilized to analyse borate glasses containing TM ions in order to determine their properties for specific applications [12–14]. Magnesium offers a variety of advantages that make it an ideal electrode material for rechargeable batteries. Magnesium batteries may be explored as lithium substitutes in the future due to their abundance, less toxicity, and environmental advantages. Magnesium batteries presently face a number of obstacles, including fewer choices of Mg intercalation cathodes due to the divalent nature of the magnesium ion and electrolyte–electrode incompatibility [15, 16]. As a result, novel cathode materials that allow reversible reactions with Mg^{2+} are desperately required. Meanwhile, various research groups have described that doping Sr^{2+} for Ba^{2+} in $LnBaCo_2O_{5+d}$ can improve the electrochemical activity of cathode materials [17–19]. This study examined the effect of doping manganese onto strontium–barium borate cathode materials, which could improve manganese ion cell performance. We have also discussed the optical, electrical, and magnetic properties of prepared glass in this paper.

2. Experimental methods

2.1 *Glass sample preparation*

A novel manganese-doped strontium barium borate (MSBB) glass was synthesized using the melt quenching technique. The glass was prepared using raw chemicals such as manganese (III) oxide (Mn_2O_3 Merck, 99% purity) as an oxidizer, boric acid (H_3BO_3 Alfa Aesar, 99.9% purity) as network former, barium carbonate ($BaCO_3$, Alfa Aeaser, 99.9% purity) and strontium oxide (SrO_3, Merck, 97.8% purity) as network modifier. The high-pure chemicals are taken in appropriate proportions ($60B_2O_3 + 20BaCO_3 + 10SrO_3 + 10Mn_2O_3$) based on the glass batch calculation. The chemical reagents were weighed in powdered form and finely ground at room temperature into a homogenous fine powder. For the fusion reaction, the required fine powder of the compositions was placed in a platinum crucible and was heated for 3 h. The obtained glass powders were melted in a muffle furnace at 1170°C, and the molten sample was put into dye at 400°C. After 4 h of the annealing process, the temperature was gradually decreased to 30°C. The sample was cut and polished from a bubble-free section and was utilized for several physical characterizations, including electrochemical analysis.

3. Result and discussion

3.1 *Powder XRD-spectrum analysis*

Figure 1 shows the powder XRD pattern of the prepared MSBB glass sample, which was performed in the range of 2θ between 20° and 80° at room temperature. In comparison to a crystal, the diffraction pattern of the amorphous solids shows a wide hump over the region rather than a sharp peak. There are no sharp peaks on the XRD pattern and a broad hump around 20–30° and
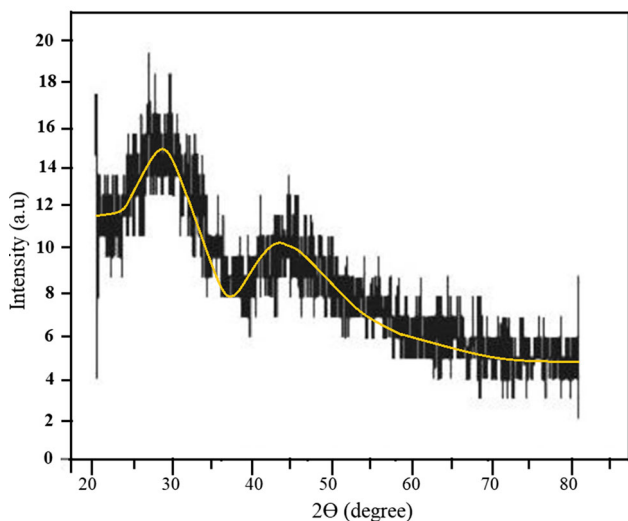
Figure 1. Powder X-ray diffraction spectrum of the MSBB glass.

40–50° (figure 1), indicates that the material is amorphous. The radial distribution function is connected to the large hump in the XRD spectrum.

3.2 *UV–Vis-NIR spectroscopic analysis*

The absorption spectrum was obtained on MSBB glass with a thickness of 2 mm using a T90 + PG spectrophotometer in the wavelength range of 200 nm to 1200 nm. The existence of different oxidation states can lead to different absorption spectra, which can be explained using ligand field theory. Manganese (II) oxide breaks down into Mn^{2+} and Mn^{3+} ions when dissolved in molten glass, resulting in a purple colour due to Mn^{3+} ions. As shown in figure 2(a), the absorption spectra of the MSBB glass have high transmittance in the range of 800 to 1200 nm, revealing the IR window characteristic. The glass sample has a substantial and wide UV absorption spectrum, with a peak at 265 nm and a broad visible band of 502 nm. The absorption band at 265 nm is associated with the $O^{2-} \rightarrow Mn^{2+}$ charge transfer transition in Mn_2O_3. The existence of trivalent manganese ion (Mn^{3+}) in octahedral sites of this glass results in an extremely wide asymmetric band located at around 500 nm [20]. The optical band-gap energy (E_g) of a glass sample was also determined using the equation [21]

$$(\alpha h\upsilon)^{1/n} = A(E_g - h\upsilon), \qquad (1)$$

where α is the optical absorption coefficient, A is the optical constant and $h\upsilon$ is the photon energy. Depending on the type of electron transition, the n value is equal to ½ or 2 for indirect and direct transition band gaps. The absorption coefficient of the sample has an energy dependency, indicating the presence of a direct band gap ($n = 2$). The variation of $(\alpha h\upsilon)^2$ vs. $h\upsilon$ in the fundamental absorption domain generates Tauc's plots for the glass sample, as shown in figure 2(b). The band-gap energy of the MSBB glass is found to be 3.51 eV using a curve extrapolated by the linear fit, intersecting at the *x*-axis on Tauc's plot. This value is comparatively equal to the manganese–borate-based glasses, and the value depends upon the concentration of boron in the glass [22]. Laorodphan *et al* [23] found that the band-gap energy of vanadate–borate glasses decreased as the boron content increased.

The linear refractive index *n* of glass is influenced by its chemical composition, as composition dictates the electrical and magnetic properties under controlled conditions. The reflectance $R(1 - T + A)$ is used to calculate the refractive index of the prepared glass, which is given by the equation [24]

$$n = \frac{\left(1 + \sqrt{R}\right)}{(1 - \sqrt{R})}. \qquad (2)$$

The wavelength dependence of the index of refraction causes material dispersion. The refractive index of most non-crystalline transparent materials decreases as the wavelength increases [25]. The refractive index (*n*) of the MSBB glass changes as a function of wavelength, as shown in figure 3(a). The refractive index steeply increases in the shorter wavelength range of 300–335 nm due to anomalous dispersion, reaching a maximum value of 2.63 corresponding to 335 nm and continuing to decrease. Normal dispersion causes the refractive index to decrease with increasing wavelength in regions of the spectrum where the material does not absorb light. The addition of Sr^{2+} to this glass network
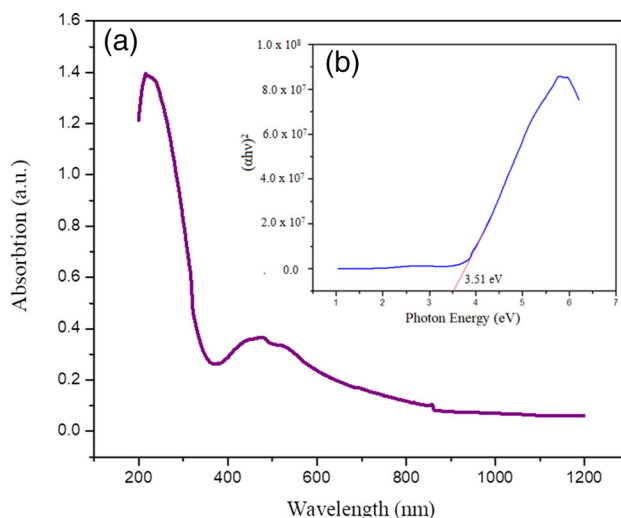

Figure 2. (a) Optical absorbance as a function of wavelength, (b) Tauc's plot: Determination of optical band-gap energy of the prepared glass.
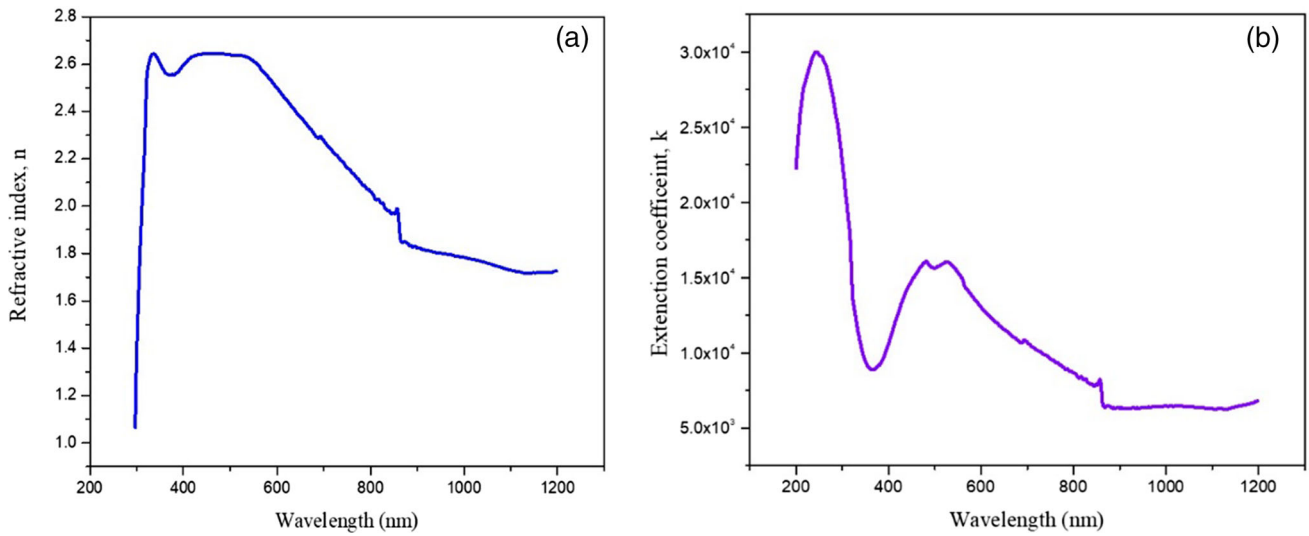
Figure 3. (**a**) Linear refractive index (n) of the MSBB glass as a function of wavelength. (**b**) Extinction coefficient (k) of the MSBB glass as a function of wavelength.

considerably increases the density, which allows light to travel at a slower rate in the medium, resulting in a higher refractive index.

The extinction coefficient (k), or imaginary part of the refractive index is a measure of how well a chemical substance absorbs light at a specific wavelength and it is derived using the Swanepoel method and the following relationship [26]:

$$k = \frac{\alpha\lambda}{4\pi}. \tag{3}$$

The optical characteristics are directly connected to the dielectric constant. The complex refractive index (N) of the medium is related as

$$N = \sqrt{\varepsilon} = n + ik, \tag{4}$$

where n is the linear refractive index, k is the extinction coefficient, and $\varepsilon = \varepsilon' + i\varepsilon''$ is the dielectric constant of the material. ε' and ε'' are the real and imaginary parts of the dielectric constant. Here, ε' represents the refraction property and ε'' shows the amount of energy absorbed owing to the electrical field of the dipole motion. As a result, these could be related as follows [27]:

$$\varepsilon_r = n^2 - k^2, \tag{5}$$

$$\varepsilon_i = 2nk. \tag{6}$$

Experiments on optical reflection, refraction and transmission are used to estimate the dielectric constant, which is linked to the band structure. Another essential feature to investigate is the conductivity of materials. The optical (σ_{op}) and electrical (σ_{e}) conductivities of the MSBB glass can be calculated using the following

formulae [28, 29]:

$$\sigma_{\mathrm{op}} = \frac{\alpha n c}{4\pi} \ (\mathrm{s})^{-1}, \tag{7}$$

$$\sigma_{\mathrm{e}} = \frac{2\lambda\sigma_{\mathrm{op}}}{\alpha} (\Omega \ \mathrm{cm})^{-1}. \tag{8}$$

Figure 3(b) shows that as the wavelength increases, the extinction coefficient (k) decreases. The extinction coefficient describes how much light is lost per unit volume due to absorption and scattering. The high k values in the lower wavelength region indicate that the glass is opaque in this region. The curve's oscillatory appearance is due to the interference effect that occurs at intermediate wavelengths. Figure 4 depicts the real and imaginary components of the dielectric constant of
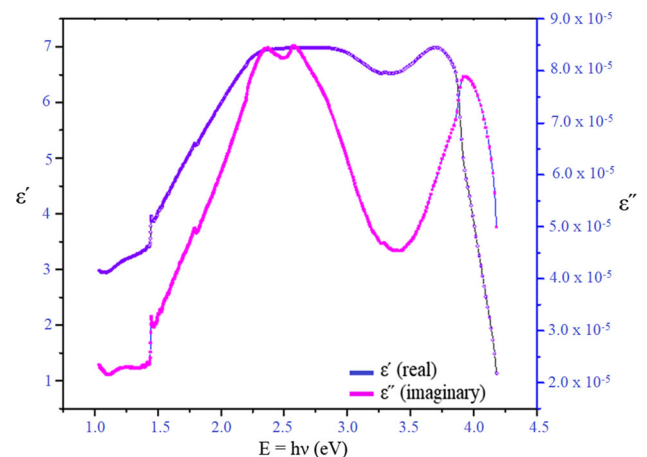

Figure 4. Real (ε') and imaginary (ε'') components of complex dielectric constant measured from optical absorbance data.
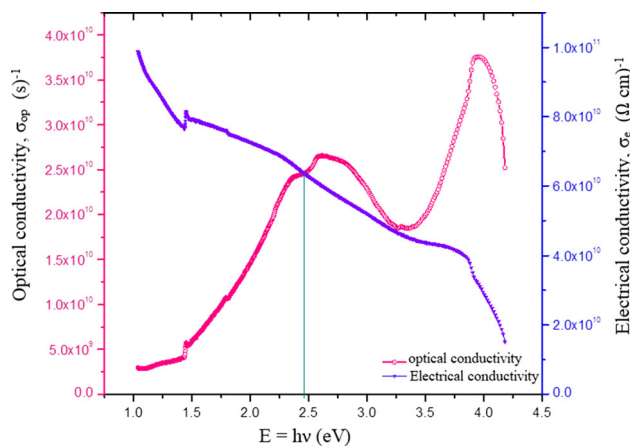
Figure 5. Optical conductivity (σ_{op}) and electrical conductivity (σ_e) as the function of photon energy.

Figure 6. FT-IR spectrum of the MSBB glass.

the MSBB glass. The variation of the real part follows a pattern that is nearly identical to the imaginary part. The imaginary part of the complex dielectric constant of the MSBB glass is found to decrease at the indirect band gap (2.45 eV) and the direct band-gap energy (3.51 eV) with the least values 8.22830×10^{-5} and 4.742×10^{-5} respectively. The decrease of ε' and ε'' at the band-gap energy region is due to the loss of energy by scattering and absorbing respectively. The ε'' increases in the photon energy ranges 1.45–2.34 eV and 3.50–3.94 eV, indicating that the loss factor increases with increasing photon energy in these regions. Whereas, a decrease of ε'' in the photon energy range 2.58–3.37 eV and above 3.94 eV indicates that the loss factor decreases with increasing photon energy in these regions.

Figure 5 shows the plots of the optical conductivity (σ_{op}) and electrical conductivity (σ_e) as a function of photon energy ($h\nu$). The indirect optical band-gap energy is calculated by intersecting σ_{op} and σ_e, and it is found to be 2.45 eV. The increase in optical conductivity is attributed to an increase in the absorption coefficient in the photon energy ranges of 1.0 to 2.5 eV and 3.4 to 3.8 eV. The peak optical conductivity curve at 2.70 eV and 3.95 eV indicate that MSBB glass has good characteristics in the visible region, and photon conduction rather than electrical conduction is the dominant mechanism. The increased optical conductivity of the prepared glass is indicated by the positive value of the σ_{op}, which is attributed to a decrease in its extinction coefficient [30]. The electrical conductivity of the glass linearly decreases as the photon energy increases (figure 5). The high σ_e of the glass at the lower photon energy domain validates its high photosensitivity. The high absorbance of glass causes a decrease in electrical conductivity, which could be produced by photon-induced electron excitation.
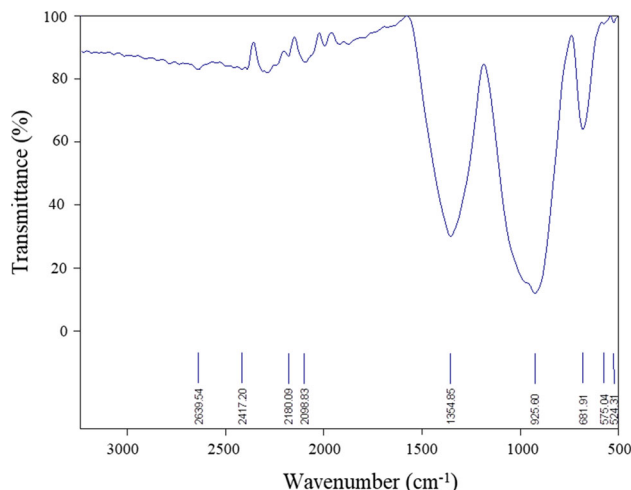
3.3 *FTIR analysis*

FTIR spectrum of prepared glasses was obtained using the KBr disc technique in the spectral region 500 to 3500 cm^{-1} and is shown in figure 6. A vibrational technique of the spectrum contains both physical and chemical states. Usually, crystalline materials have sharper bands than the spectrum of amorphous/no-crystalline material. The peaks at 524 cm^{-1} represent the vibrations of the Mn–O bond and metal cations Sr^{2+}. The peak was observed at 575 cm^{-1} due to the specific vibration of Ba–O bonds' low intensity. The peak at 925 cm^{-1} corresponds to B–O–B bending vibrations, which are caused by an oxygen bridge between trigonal and tetrahedral boron atoms. The fundamental stretching of B–O–B was observed at 1354 cm^{-1}. The peak at 1996 cm^{-1} was attributed to B–O stretching vibration of trigonal BO$_3$ units in the boroxol ring. The band between 2098 and 2639 cm^{-1} is ascribed to hydrogen bonding and/or water vibrations or BOH [31].

3.4 *Dielectric analysis*

Dielectric characteristics emerge from ionic movements in ionic conducting glasses. Charge carriers cannot easily move through the glass structure, but they can be transformed and polarized by an applied electric field. The dielectric characteristics are influenced by two mechanisms: (i) ions spinning about their negative sites, and (ii) short-range transport (hopping). The dielectric constant (ε') and the dielectric loss tangent (tan δ) of the MSBB glass have been obtained using the following formula in the frequency range of 100 Hz to 5 M Hz at room temperature [32]:

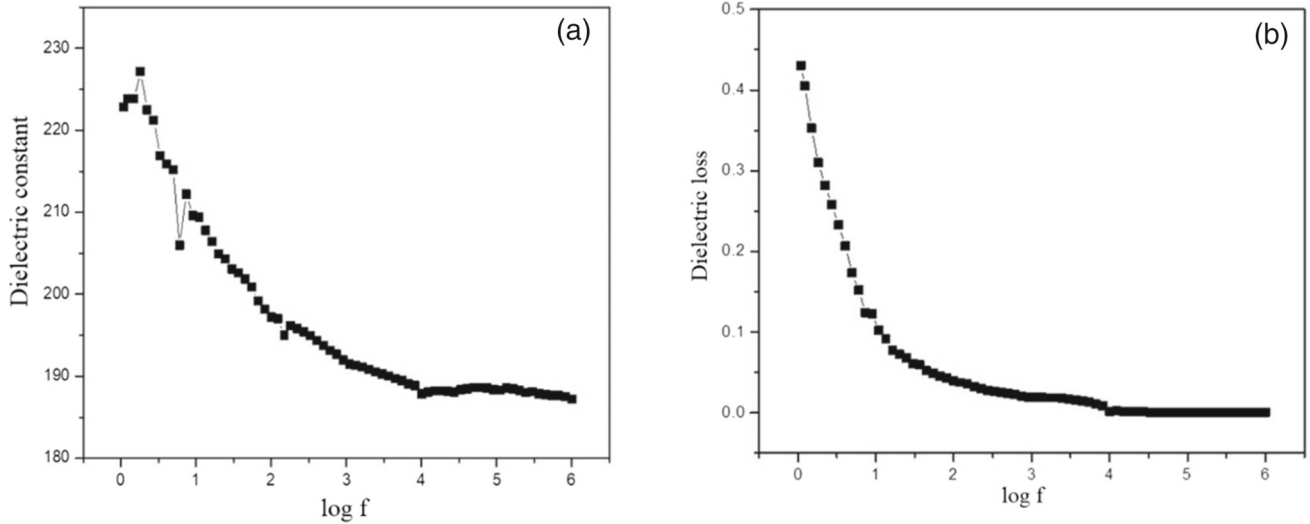$$\varepsilon' = \frac{C_p t}{\varepsilon_0 A}, \tag{9}$$

Figure 7. (**a**) Dielectric constant (ε_r) and (**b**) dielectric loss tangent (tan δ) as a function of frequency.

$$\tan \delta = \frac{\varepsilon''}{\varepsilon'}, \tag{10}$$

where C_p is the sample capacitance, ε_o is the free space permittivity, and A is the cross-sectional area. The ac conductivity (σ_{ac}) of the glass is determined from the dielectric values using the following formula [32]:

$$\sigma_{ac} = 2\pi \nu \, \varepsilon_o \varepsilon_r \tan \delta, \tag{11}$$

where ε_0 is the permittivity of free space, t is the thickness of the glass sample, and ν is the frequency of the applied field. The influence of frequency on the dielectric constant has been studied for the glass sample, as shown in figure 7(a). With increasing frequency, the dielectric constant decreases exponentially, and the large value of the dielectric constant in low frequencies is owing to the dominance of space charge polarization in this domain. The variation in dielectric constant can be described by space-charge polarization, which is caused by the existence of greater conductivity phases in a glass structure, resulting in localized charge accumulation under the influence of an applied electric field. The contribution of various oxidation states of manganese ($Mn^{2+/3+}$), Sr^{2+}, and Ba^{2+} ions to the host structure generate enough dipoles which lead to the high dielectric constant (~ 228). The alignment of axes parallel to an alternating electric field takes a finite amount of time for space-charge carriers, including ionic and electronic carriers, which are present in the glass. All charge carriers will be unable to keep up with the field as the frequency of the field increases, and their direction will lag behind the fields. As a result, the dielectric constant of the material decreases.

In figure 7(b), the dielectric loss was likewise shown to decrease with frequency. As a result, changes in

the electronic exchange process have an impact on the conduction process and dielectric mechanism. The interfacial polarization process is responsible for the large dispersion of the dielectric loss tangent at low frequencies. The dielectric loss decreases exponentially with a trailing rim as frequency increases due to the low reactance given by the prepared glass, which causes reduced involvement of ions in the electric field direction. Moving charges may also be responsible, as they dominate polarisation in low-frequency regions and have low dipolar relaxations in high-frequency regions.

The ac conductivity of the MSBB glass as a function of frequency is depicted in figure 8. At lower frequencies, conductivity is frequency-independent, but it rises sharply as a function of higher frequencies.
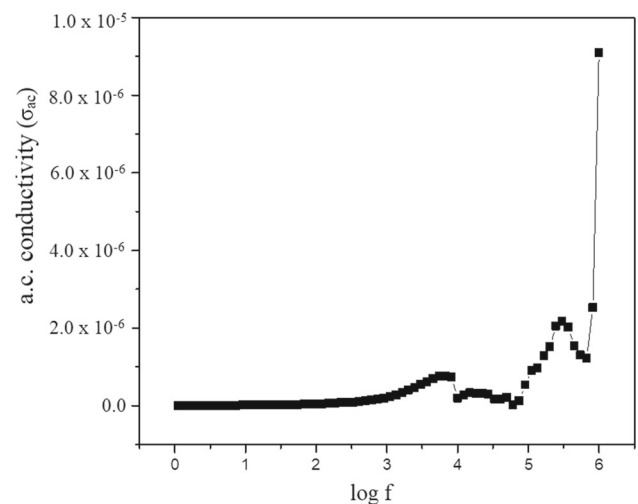

Figure 8. The ac conductivity (σ_{ac}) of the MSBB glass as a function of frequency.

Because of the high energy barrier in the low-frequency region, fewer charge carriers with lengthy relaxation times respond, resulting in low conductivity [33]. As a result of the lower energy barrier height at higher frequencies, a greater proportion of charge carriers respond quickly and have short-range Mn^{2+} ion movement due to the shorter time periods available, resulting in increased conductivity. Furthermore, the conductivity of glass medium is independent of frequency at lower frequencies, and this is considered as dc conductivity at low frequencies which is related to the random distribution of ionic charges (Sr^{2+}, Mn^{2+}, and Mn^{3+}) caused by activated hopping, whereas conductivity at higher frequencies is due to the dispersion that increases linearly in the higher frequency zone ($\sigma_{dc} = 0$). The increasing pattern of ac conductivity as frequency rises could be related to cation disorder in their locations, as well as due to the presence of space charge [34].

In addition, the presence of solid electrodes acting as blocking surfaces on the charge carriers causes noticeable alterations in the complex conductivity function at lower frequencies. Because the metal electrode blocks the ions, they accumulate or deplete near the electrodes, forming space-charge layers [35, 36]. The voltage in these layers declines rapidly, implying that the material is highly polarised electrically and that the bulk sample has no electric field at low frequencies. With decreasing frequency, the accumulation of electrical polarization and decrease in the electric field in the bulk are expressed in an increase in the ac permittivity and a decrease in the ac conductivity.

3.5 *Vibrating sample magnetometer study*

The magnetic characteristics of the MSBB glass were determined using a vibrating magnetometer (VSM, Lakeshore 7410) under $\pm$ 15 kOe at room temperature. The magnetization of the prepared glass increases linearly with the applied magnetic field, and the curve does not reach saturation until a field of 15 kOe is applied, as shown in figure 9. This is due to dipole surface spins that do not rotate incompatible with the magnetic moment and hence do not saturate as quickly as the core when the field increases.

The manganese ion appears as Mn^{3+} in borate glasses with octahedral coordination, which has substantial magnetic anisotropy due to its intense spin–orbit interaction with the 3d orbital [37]. Mn^{2+} and Mn^{3+} are well-known paramagnetic ions, whereas Mn^{2+} and Mn^{4+} are luminous activators, respectively [38]. The addition of Sr^{2+} and $Mn^{2+/3+}$ ions to various sites of borate disturbed its structure and led to the formation of more dipoles, such as Sr–O, Mn–O and Ba–O. The saturation magnetisation (M_s) is high since there are more dipoles
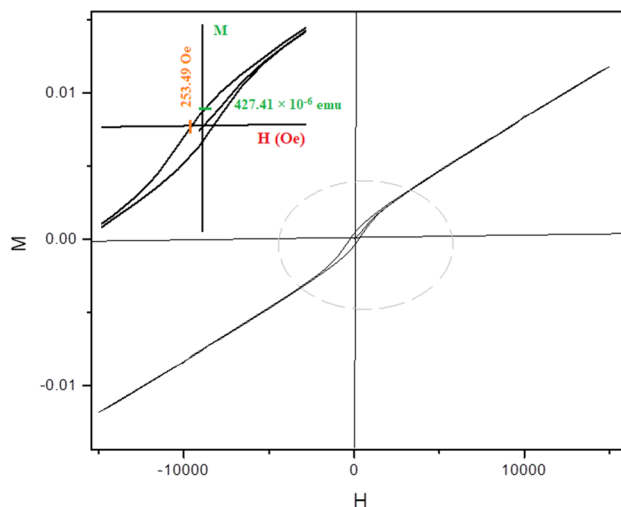

Figure 9. Hysteresis curve: Magnetization (M) vs. magnetic field (H).

randomly dispersed at zero magnetising force. When the glass sample is placed in a magnetic field, the increase in M_s with increasing dopant (Sr^{2+}, $Mn^{2+/3+}$) concentration could be attributed to an increase in unpaired electrons, which produce a substantial net magnetisation [39]. From the hysteresis loop of the MSBB glass, the magnetic parameters such as remanent magnetisation (M_r) and coercivity were found to be 427.41×10^{-6} emu (at $H = 0$) and 253.49 Oe (at $M = 0$), respectively. A small remanent magnetisation and coercive fields are known to be observable on the loop due to its grain size and the presence of impurities in the glass, especially interstitial components like C and O. The hysteresis curve of this glass is narrow in size and has a lower surface area, indicating that it has paramagnetic features.

3.6 *Electrochemical properties*

The MSBB glass electrode was subjected to cyclic voltammetry and electrochemical impedance spectroscopy (EIS) utilizing a Solartron 1287 electrochemical interface and a 1255B FRA. The cyclic voltammogram (CV) was performed on the MSBB electrode in a 5 M KOH electrolyte with a scan rate of 1 m/V for 10 cycles. The potassium hydroxide (KOH) electrolyte was chosen for its long-lasting ionic conductivity, high OH^- anion mobility in aqueous solutions, and small size. When the concentration of KOH rises, the number of ions in the electrolyte rises as well, increasing the electrolyte's ionic conductivity. The following equation is used to estimate the specific capacitances of the electrodes using cyclic voltammetry (CV) [40–42]:

$$C_{CV} = \frac{1}{mv\Delta V} \int I dV, \tag{12}$$

where m is the mass of the active materials (g), I is the response current (A), υ is the scan rate (mV s^{-1}), and ΔV is the potential window (V). In a galvanostatic charge–discharge study, the equation was used to determine the electrode's specific capacitance (CGCD):

$$C_{sp} = \frac{I \Delta t}{m \Delta V},\tag{13}$$

where I is the discharge current (A), ΔV is the potential window (V), Δt is the discharge time, and m is the mass of the active materials (g). The power density (P) and energy density (E) for the electrodes have been estimated using the relation [43]

$$E = C_{GCD}\frac{\Delta V^2}{7.2}\ (\text{Wh/kg}),\tag{14}$$

$$P = E \times \frac{3600}{t}(\text{W/kg}),\tag{15}$$

where t is the discharge time (s), ΔV is the potential window and CGCD is the specific capacitance determined from charge–discharge measurement (F/g). The current at the working electrode is measured during the potential scans to produce a cyclic voltammogram as shown in figure 10. It has been observed that as the scanning rate increases, the current density increases. In a voltage range of –1.0 to 1.5, cyclic voltammetry was investigated. The reduction process takes place in the switching potential region of –0.49 to 0.0 V, and the potential is scanned negatively in this region, resulting in a reduction (discharging). The reduction peak potential is observed when all of the ions (Sr^{2+}, Mn^{2+} and Mn^{3+}) at the surface of the electrode have been reduced, and it is found to be –0.74 V. During the reduction process, granular particles can offer more interfacial area contact inside a KOH electrolyte. As a result, an increase in the probability of the Mn^{2+} ions intercalating back into the host structure offers a high Coulomb potential. After the reduction process, the potential scan starts positively from 0.0 to 0.5 V. The peak potential is attained to its maximum when all of the substrate ions on the surface of the electrode have been oxidized. During oxidation and reduction, the electrolytic solution provides ions to the electrodes. According to the CV, the glass shows a greater oxidation potential peak at 100 mV/s than at other scan rates. The oxidation (charging) procedure reveals that the smaller the particle size, the higher the potential required to extract manganese ions [44]. The CV curve of the glass sample displays a couple of redox peaks, which is a common method of pseudo-capacitance that involves the process of electroactive ion (Mn^{2+} and Mn^{3+}) absorption on the electrode material surface for charge transfer through faradaic reactions [45].

The prepared glass electrode's specific capacitance was calculated as a function of current density from 0 to 20 A/g. As shown in figure 11(a), the MSBB glass electrode has a specific capacitance of 84 F g^{-1} at a current density of 2 A g^{-1} and decreased to 53 F g^{-1}. The glass sample has the highest specific capacitance due to the strongest redox reaction in the Mn oxidation state. The large-sized Ba^{2+} cations in the glass structure, which partially occupy tunnel cavities at specific stable lattice sites, are expected to interact with charge carriers (Mn^{2+} and Mn^{3+}) and hence affect electrode charge storage capacity [46, 47]. The glass has a relatively high specific capacitance when compared to lithium manganese borate glasses [48]. The specific capacitance of the prepared glass electrode decreases as the current density increases because the electrolyte ion does not have enough time to penetrate deep into the pores of the material. Furthermore, the glass sample could have a high redox reaction [49]. The energy density produced under relatively high power density conditions is a vital measure to evaluate the actual performance of practical supercapacitors. The ions in the electrolyte can diffuse/penetrate into microscopic holes, hence a large microscopic volume can help to store charge and increase total capacity. In the meso- and micro-porous area, however, hierarchical pores provide unobstructed channels for fast ion transport. The power density vs. energy density of the MSBB glass is shown in figure 11(b). A high power density does not always imply a high energy density. A glass sample with high energy but low power density can work for an incredible duration. The glass exhibits a high power density with low energy density, indicating that it can quickly release and recharge energy.

Electrochemical impedance spectroscopy (EIS) was used to determine equivalent circuit parameters such as ohmic resistance (R) and charge transfer resistance (R_{ct}). Figure 12 shows the Nyquist plot of the MSBB glass impedance between Z' and Z''. The Nyquist plot reveals a deformed semi-circle in the high-frequency zone due to the absorbency of the electrode, and a perpendicular linear slope in the low-frequency zone, indicating ideal capacitive behaviour. In the magnified high-frequency area, however, there are noticeable variances among the curves (figure 12, inset). The value of ohmic resistance (R) is calculated by the high-frequency intercept of a semi-circle on the real axis (Z'), and it is found to be 17.7 Ω for this glass electrode. The charge transfer resistance was determined to be 36.10 Ω cm^2 on the enlarged Nyquist plot of the glass sample, and it was associated with the diameter of the semicircle. A lower charge transfer and more effective electrolyte accessibility within the structures are shown by a smaller semicircle diameter and a shorter 45° Warburg region.
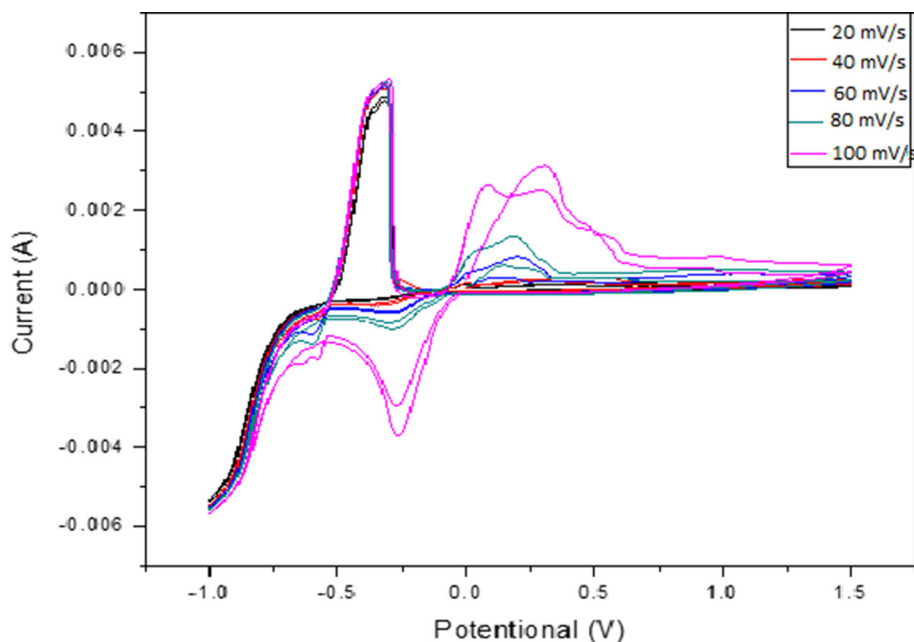
Figure 10. Cyclic voltammogram: Pseudo-capacitive characteristic of the MSBB glass electrode determined from the potential vs. current with various scan rates.
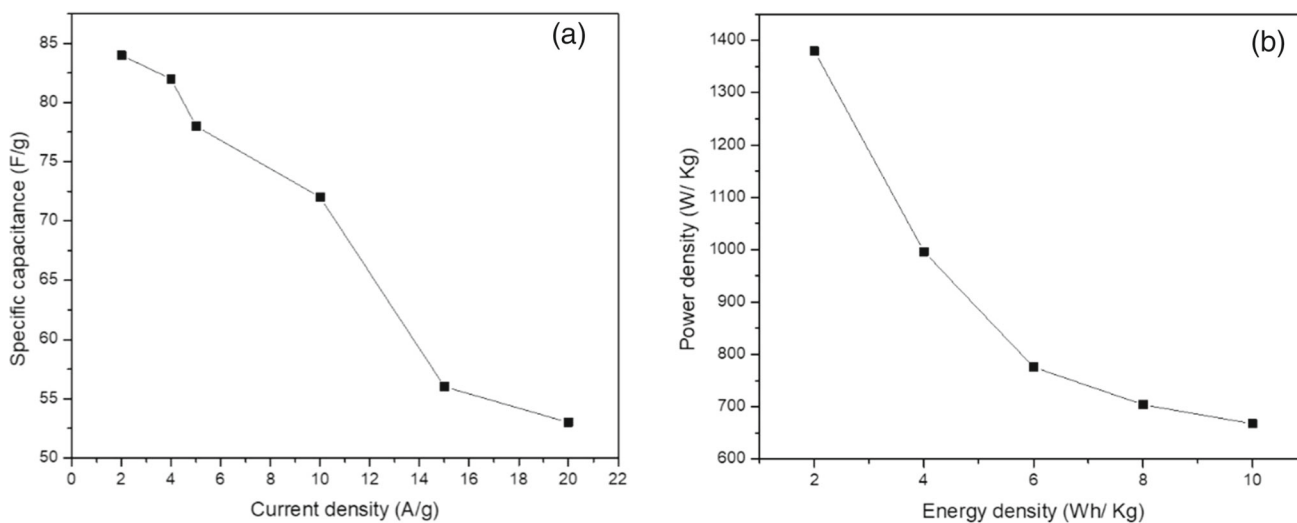

Figure 11. (**a**) The specific capacitance of the MSBB glass as a function of current density. (**b**) The power density of the MSBB glass as a function of energy density.

According to the findings obtained, the prepared MSBB glass has a high potential for use in supercapacitor applications.

3.7 *Microhardness study*

Hardness measurement is used to find the mechanical stability of the materials and materials category. The micro-hardness test was carried out on MSBB borate glass at 30°C using Vicker's hardness tester with a loading range of 10–200 g. The load was applied to the sample with a dwell time of 10 s and the corresponding indentation length was measured. The H_v is calculated for each corresponding load using the following equation [50]:

$$H_v = \frac{1.8544P}{d^2} \text{ kg/mm}^2, \tag{16}$$

where P is the applied load in kg, H_v is the Vicker's hardness number, and d is the average diagonal length of the indentation mark. The yield strength is a measure of stress required to start deforming a material plastically,
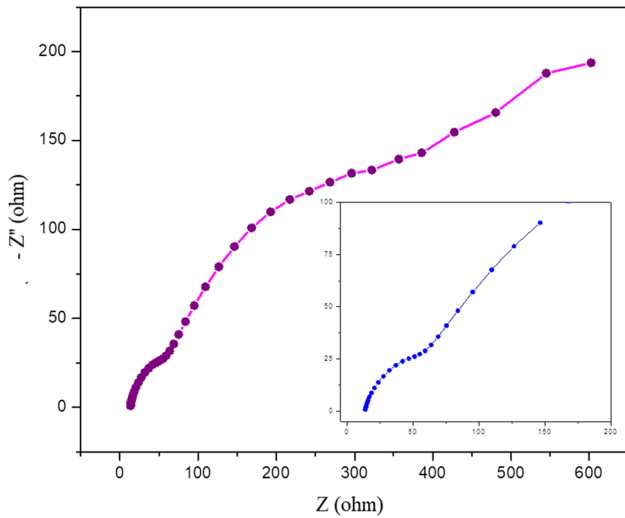
Figure 12. Nyquist plot: The relation between the real and imaginary components of impedance (inset: high-frequency zone).

Figure 14. Stiffness constant (C_{11}) and c/a of the MSBB glass as a function of applied loads.

and the relation is used to calculate it is

$$\sigma_y = \frac{H_v}{3} \, \text{kg/mm}^2. \tag{17}$$

Figure 13 represents the load relative to the yield strength and hardness number of the MSBB glass. The magnitude of the microhardness number depends on the applied load. As a result of the measurement, H_v increases with increasing load values demonstrating the reverse indentation size effect (RISE). The crack occurred beyond 100 g, indicating that the glass system experienced stress-related dislocations. The glass is subjected to both shear and compression throughout the measurement, which has an effect on the plastic
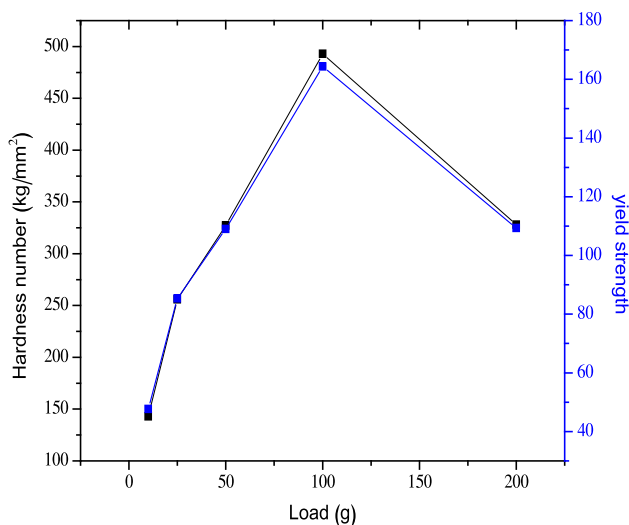
flow, densification, and elastic deformation caused by the applied load. The yield strength of the MSBB glass was found to increase by varying the load. The Meyer's index value (n) of the MSBB glass was estimated from Mayer's relation, $P = k_1 d^n$ [51]. According to Onitsch, if n is less than 1.6, the material belongs to the hard material type. If n is more than 1.6, the compound is a soft material. The MSBB glass has an n value of 2.5, indicating that it belongs to the soft material category.

The elastic stiffness constant (C_{11}) for MSBB glass was estimated using Wooster's empirical formula $C_{11} = H^{7/4}$. The stiffness constants of the MSBB glass vary with applied load up to 100 g, revealing that the bonding force between the ions is more rigid, as shown in figure 14. The fracture toughness (K_c) and Brittle index (B_i) of the glass were calculated using the following equation [52, 53]:

$$K_c = \frac{P}{\beta_o C^{3/2}} \, \text{MPa m}^{-1/2} \tag{18}$$

$$B_i = \frac{H_V}{K_c} \, \text{m}^{-1/2}, \tag{19}$$

where C is the crack length measured, β_o is taken as 7 for Vickers's indenter and P is the applied load in kg. Figure 15 shows the loads related to the fracture toughness and brittle index of MSBB borate glass. As the applied loads increase, the fracture toughness increases and the brittle index decreases. Fracture toughness can be related to Young's modulus and bond strength of the glass material. The breakage of the weakest bonds between modifying cations and non-bridging oxygen occurred due to the cracks. The fracture induces brittleness and thus affects the mechanical property of the
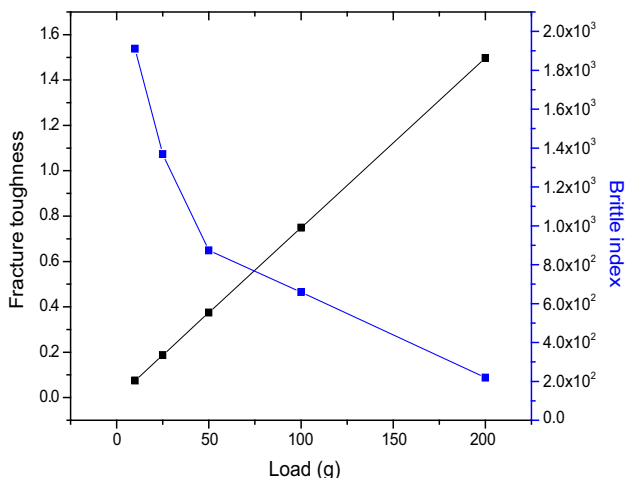

Figure 13. Hardness number (H_v) and yield strength (σ_y) of the MSBB glass as a function of applied loads.

Figure 15. Fracture toughness (K_c) and brittle index (B_i) of the MSBB glass as a function of applied loads.

MSBB borate glass, which reveals that MSBB glass has good brittle index. In brittle materials, propagating cracks produced fracture at the four corners of the indentation which frequently originates from flaws and extends during above-threshold stress.

3.8 *Scanning electron microscopy analysis*

The microstructure of the prepared glass was carried out using Mini SEM Hirox SH-400 M. The SEM topog-

raphy of the MSBB glass illustrates rough and coarse morphology of the particles. Figure 16 shows the SEM topography of the borate glass with different magnification: (a) 400 μm, (b) 10 μm, (c) 5 μm, and (d) 1 μm. The SEM images of the MSBB glass demonstrates a clear surface without any microstructure, which confirms the amorphous nature of the material.

3.8.1 *Gamma ray shielding features.* The GM counter is used to determine the magnitude of γ-ray absorption by the prepared glass. The γ-ray source was a ^{60}Co cell operating at 32°C with a dosage rate of 150 rad/s. The measurement recorded the intensity of transmitted radiation resisted by the glass. The count for the prepared glass sample was computed to be 900 (1150), with the figure in the bracket indicating background counts. The mass attenuation coefficient (μ/ρ), half-value layer (HVL) and mean free path (MFP) of the MSBB glass were calculated in the range of 0.01–15 MeV using Phy-X software. The variation of the mass attenuation coefficient of the prepared glass as a function of photon energy is depicted in figure 17. The value of the mass attenuation coefficient (μ/ρ) increases till the photon energy reaches 0.04 MeV, and a further increase in photon energy shows that the μ/ρ value starts decreasing and attains saturation. This result reveals that at lower energies, the γ-photon has a greater possibility of interaction with the studied glass, and there is a substantial
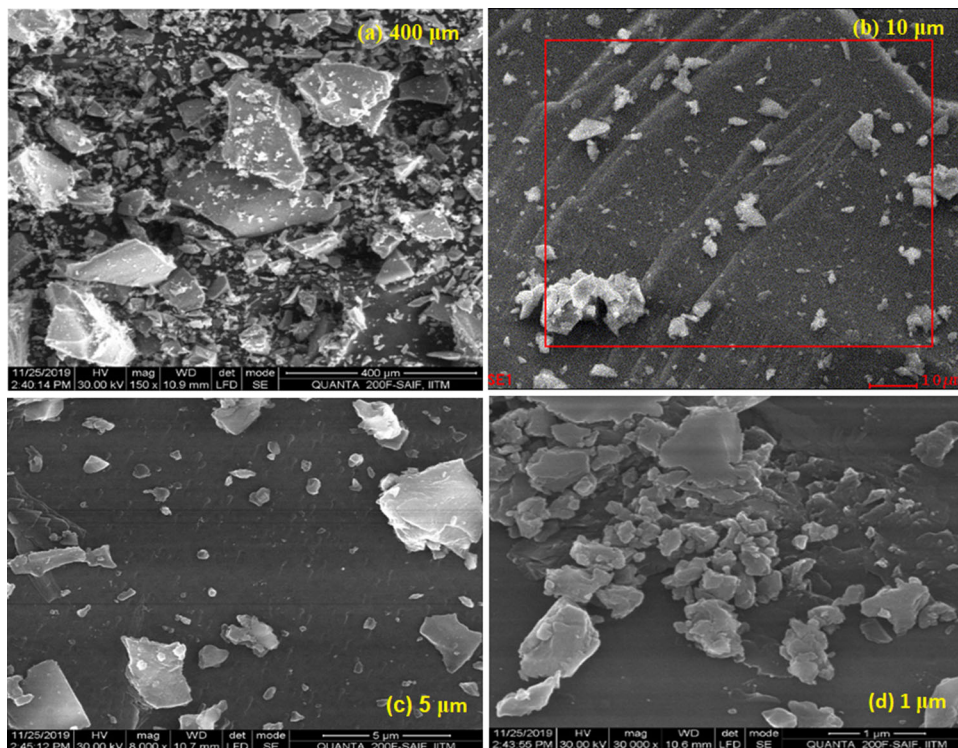

Figure 16. SEM topography of the MSBB glass with different magnification: (**a**) 400 μm, (**b**) 10 μm, (**c**) 5 μm and (**d**) 1 μm.
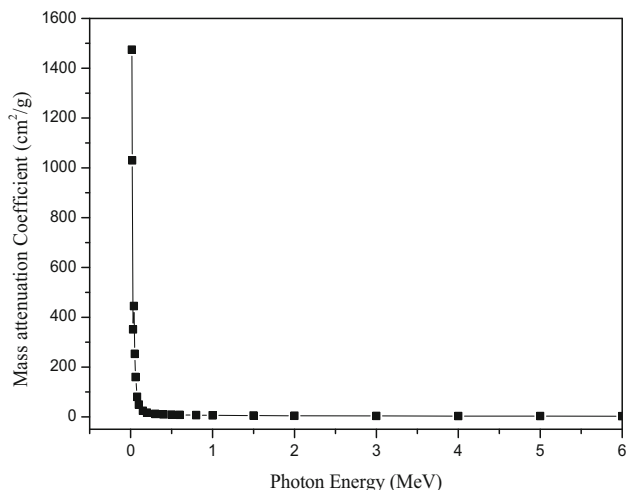
Figure 17. Mass attenuation coefficient (μ/ρ) of the MSBB glass as a function of photon energy.

Figure 18. Half-value layer (HVL) and mean free path (MFP) of the MSBB glass as a function of photon energy.

attenuation due to the photoelectric absorption mechanism's dominance. As the energy rises, photoelectric absorption becomes less feasible, and other interactions such as Compton scattering and pair formation become more dominant [54].

The HVL is the thickness of the material required to reduce the intensity of the incident photon beam to half its initial value of the incident photon. The average distance travelled by a photon between two consecutive scattering/collisions in the material is measured by the mean free path. The following equations were used to determine the HVL and MFP:

$$\text{HVL} = \frac{0.693}{\mu}, \tag{20}$$

$$\text{MFP} = \frac{1}{\mu}, \tag{21}$$

where μ refers to the fraction of photons that are absorbed or scattered per unit thickness of the glass sample. A high value of μ suggests that only a small quantity of photons pass through the glass. Figure 18 demonstrates the variation of HVL and MFP as a function of photon energy.

4. Conclusion

A novel manganese-based cathode glass material (MSBB) has been successfully prepared by utilizing the melt quenching technique. The powder-XRD analysis of the prepared glass revealed no evidence of crystallinity, confirming the amorphous nature of the sample. In an optical absorption spectrum of the prepared glass, λ_m of Mn^{3+} ion was discovered to be 502 nm. The optical conductivity of the glass is entirely positive, and two peaks
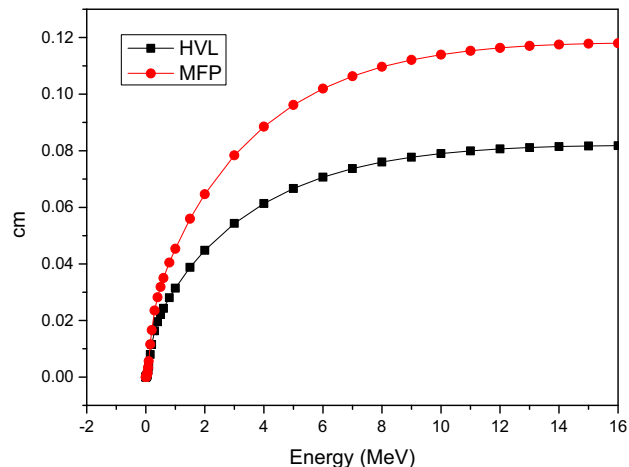
observed in the optical conductivity spectrum reveal the interior penetration of the electromagnetic wave. The high electrical conductivity at lower photon energy validates the remarkable photosensitivity of the glass. Dielectric characteristics are reported to be decreasing as ac conductivity increases with frequency due to the hopping of electrons between different valence states. The VSM result indicates that the glass has paramagnetic properties, and the hysteresis curve does not show saturation up to the applied field of 15 kOe. The cyclic voltammogram curve displays pseudo-capacitive behavior, indicating that Mn^{2+}/Mn^{3+} is in a mixed oxidation state. The glass electrode has the highest specific capacitance value of 84 F g^{-1}, indicating that it could be a potentially promising glass electrode in future Mn-ion batteries. The mechanical behavior of the prepared glass was studied with different loads. The microstructure of the prepared glass was analysed. The prepared glass was investigated for shielding parameters such as μ/ρ, MFP, and HVL, and the findings demonstrated that the glass is a potential material for gamma ray shielding applications.

References

[1] E Mansour, G M El-Damrawi, Y M Moustafa, S Abel El Maksoud and H Doweider, *Phys. B: Condens. Matter* **293**, 268 (2001), https://doi.org/10.1016/S0921-4526(00)00559-7

[2] S Afyon, F Krumeich, C Mensing, A Borgschulte and R Nesper, *Sci. Rep.* **4**, 7113 (2014), https://doi.org/10.1038/srep07113.

[3] Kawa M Kaky, M I Sayyed, Abbas Khammas, Ashok Kumar, Erdem Şakar, Alyaa H Abdalsalam, Betül Ceviz Şakar, Bünyamin Alim and M H A Mhareb, *Mat. Chem.*

Phys. **242**, 122504 (2020), https://doi.org/10.1016/j.matchemphys.2019.122504

[4] O V Mazurin, M V Streltsina and T P Shvaiko-Shvaikovskaya, *The Properties of the Glasses and Glass-Forming Melts* (Nauka, Leningrad, 1977) vol. 3

[5] T S Markova, O V Yenush, I G Polyokova and B Z Pevzner, *Phys. Chem. Glasses. Eur. J. Glass Sci. Technol.* **47**, 476 (2006)

[6] E I Kamitsos, *Phys. Chem. Glasses* **44**, 79 (2003)

[7] R S Kaundal, Sandheep Kaur, Narveer Singh and K J Singh, *J. Phys. Chem. Solids* **71**(**9**), 1191 (2010), https://doi.org/10.1016/j.jpcs.2010.04.016

[8] K Annapoorani, N Suria Murthy, T R Ravindran and K Marimuthu, *J. Lumin.* **171**, 19 (2016), https://doi.org/10.1016/j.jlumin.2015.10.071

[9] J Krogh-Moe, *Phys. Chem. Glasses* **6**, 46 (1965)

[10] S Amudha, J Ramana Ramya, K Thanigai Arul, A Deepika, P Sathiamurthi, B Mohana, K Asokan, Chung-Li Dong and S Narayana Kalkura, **196**, 108099 (2020), https://doi.org/10.1016/j.compositesb.2020.108099

[11] V Karageorgiou and D Kaplan, *Biomaterials* **26**(**27**), 5474 (2005), https://doi.org/10.1016/j.biomaterials.2005.02.002

[12] I Konidakis, Christos-Platon E Varsamis, E I Kamitsos, D Möncke and D Ehrt, *J. Phys. Chem. C* **114**, 9125 (2010), https://doi.org/10.1021/jp101750t

[13] A Winterstein, H Akamatsu, D Möncke, K Tanaka, M A Schmidt and L Wondraczek, *Opt. Mater. Express* **3**,184 (2013), https://doi.org/10.1364/OME.3.000184

[14] U Selvaraj and K J Rao, *Spectrochim. Acta A Mol. Biomol. Spectrosc.* **40**, 1081 (1984), https://doi.org/10.1016/0584-8539(84)80137-3

[15] M Mesallam, E Sheha, E M Kamar and N Sharma, *Mater. Lett.* **232**, 103 (2016), https://doi.org/10.1016/j.matlet.2018.08.080

[16] S Son, T Gao and S P Harvey, *Nat. Chem.* **10** 532 (2018), https://doi.org/10.1038/s41557-018-0019-6

[17] J Zhao, *Environ. Sci. Technol.* **33**, 2081 (1999), https://doi.org/10.1021/es9807643

[18] Hidefumi Odaka, Shuichi Iwata, Naoaki Taga, Shuhei Ohnishi, Yasunori Kaneta and Yuzo Shigesato, *Japanese J. Appl. Phys.* **36**, 5551 (1997), https://doi.org/10.1143/JJAP.36.5551

[19] P Qu, J Zhao, T Shen and H Hidaka, *J. Mol. Catal. A Chem.* **129**, 257 (1998), https://doi.org/10.1016/S1381-1169(97)00185-4

[20] J B Macctre, E F Lopez, J Gallardo-Amores, R R Casero, V S Escribano and E P Bernal, *Int. J. Inorg. Mater.* **3**, 889 (2001), https://doi.org/10.1016/S1466-6049(01)00091-5

[21] M Dhavamurthy, P Vinothkumar, A Antony Suresh, Manoj Mohapatra and Priya Murugasen, *Results in Optics* **8**, 100232 (2022), https://doi.org/10.1016/j.rio.2022.100232

[22] Amorntep Montreeuppathum, Pinit Kidkhunthod, Saroj Rujirawat, Rattikorn Yimnirun, Supree Pinitsoontorn and Santi Maensiria, *Radiat. Phys. Chem.* **170**, 108677

(2020), https://doi.org/10.1016/j.radphyschem.2019.108677

[23] N Laorodphan, P Pooddee, P Kidkhunthod, P Kunthadee, W Tapala and R Puntharod, *J. Non-Cryst. Solids* **453**, 118 (2016), https://doi.org/10.1016/j.jnoncrysol.2016.10.005

[24] M Dhavamurthy, S V Vijayasundaram and N Jeni Victor, *Glass Phys. Chem.* **47**, S21 (2021), https://doi.org/10.1134/S108765962107004X

[25] L N Thibos, A Bradley, D L Still and X Zhang, *Vision Res.* **30**(**1**), 33 (1990), https://doi.org/10.1016/0042-6989(90)90126-6

[26] R Swanepoel, *J. Phys. E: Sci. Instrum.* **16**, 1214 (1983), https://doi.org/10.1088/0022-3735/16/12/023

[27] A Goswami, *Thin film fundamentals* (New Age International, New Delhi, 2005)

[28] U Kara, S A M Issa, N Y Yorgun, O Kilicoglu, M Rashad, M M Abuzaid and H O Tekin, *J. Non-Cryst. Solids* **539**, 120049 (2020), doi:https://doi.org/10.1016/j.jnoncrysol.2020.120049

[29] H A ElBatal, F H ElBatal and A M Abdelghany, *The Open Spectroscopic J.* **8**, 1 (2014)

[30] P Sharma and S C Katyal, *J. Phys. D: Appl. Phys.* **40**, 2115 (2007), https://doi.org/10.1088/0022-3727/40/7/038

[31] M A Marzouk, F H ElBatal, W H Eisa and N A Ghoneim, *J. Non-Cryst. Solids* **387**, 155 (2014)

[32] P Vinothkumar, M Dhavamurthy and Manoj Mohapatra, *Bull. Mater. Sci.* **44**, 257 (2021), https://doi.org/10.1007/s12034-021-02545-9

[33] V Naresh and S Buddhudu, *J. Ferroelectrics* **437**, 110 (2012), https://doi.org/10.1080/00150193.2012.741987

[34] Tasiu Zangina, Jumiah Hassan, Khamirul Amin Matori, Raba'ah Syahidah Azis, Umaru Ahmadu and Alex See, *Results Phys.* **6**, 719 (2016), https://doi.org/10.1016/j.rinp.2016.10.003

[35] A A Khamzin, I I Popov and R R Nigmatullin, *Phys. Rev. E* **89**, 032303 (2014) https://doi.org/10.1103/PhysRevE.89.032303

[36] P B Macedo, C T Moynihan and R Bose, *Phys. Chem. Glasses* **13**, 171 (1972)

[37] D Beeman, R Lynds and M R Anderson, *J. Non-Cryst. Solids* **42**, 61 (1980), https://doi.org/10.1016/0022-3093(80)90008-3

[38] Aldert van der Ziel, *Solid State Physical Electronics* (Prentics Hall of India, New Delhi, 1997)

[39] R M Khattab, H E H Sadek and A A Gaber, *Ceram. Int.* **43**, 234 (2017), https://doi.org/10.1016/j.ceramint.2016.09.144

[40] B S Benila, K C Bright, S Mary Delphine, R Shabu, *J. Magn. Magn. Mater.* **426**, 390 (2017), https://doi.org/10.1016/j.jmmm.2016.11.120

[41] J Elberin Mary Theras, D Kalaivani, J Arul Martin Mani, D Jayaraman and V Joseph, *Opt Laser Technol.* **83**, 49 (2016), https://doi.org/10.1016/j.optlastec.2016.03.027

[42] J Gomez and E E Kalu, *J. Power Sources* **230**, 218 (2013), https://doi.org/10.1016/j.jpowsour.2012.12.069

[43] J Khajonrit, U Wongpratat, P Kidkhunthod, S Pinitsoon-torn and S Maensiri, *J. Magn. Magn. Mater.* **449**, 423 (2018), https://doi.org/10.1016/j.jmmm.2017.10.092

[44] Chung-Hsin Lu and Shang-Wei Lin, *J. Power Sources* **97**, 458 (2001), https://doi.org/10.1016/S0378-7753(01)00637-1

[45] Jilei Liu, Jin Wang, Chaohe Xu, Hao Jiang, Chunzhong Li, Lili Zhang, Jianyi Lin, and Ze Xiang Shen, *Adv. Sci.* **5(1)**, 1700322(9) (2017), https://doi.org/10.1002/advs.201700322

[46] Dengyun Zhai, Baohua Li, Chengjun Xu, Hongda Du, Yanbing He, Chunguang Wei and Feiyu Kang, *J. Power Sources* **196**, 7860 (2011), https://doi.org/10.1016/j.jpowsour.2011.05.015

[47] Y Yuan, Anmin Nie, G M Odegard, Rui Xu, D Zhou, S Santhanagopalan, Kun He, Hasti Asayesh-Ardakani, D D Meng, R F Klie, C Johnson, J Lu and R Shahbazian-Yassa, *Nano Lett.* **15**, 2998 (2015), https://doi.org/10.1021/nl5048913

[48] P Butnoi, N Chanlek, Y Poo-arporn, S Pinitsoontorn, S Maensiri and P Kidkhunthod, *J. Alloys Compd.* **809**, 151811 (2019), https://doi.org/10.1016/j.jallcom.2019.151811

[49] R Mondal, S Sahoo and C S Rout, *Am. J. Eng. Appl. Sci.* **9(3)**, 540 (2016), https://doi.org/10.3844/ajeassp.2016.540.546

[50] C Balarew and R Dehlew, *J. Solid State Chem.* **55**, 1 (1984), doi:https://doi.org/10.1016/0022-4596(84)90240-8

[51] V Raja, A K Sharma and V V R Narasimha, *Mater. Lett.* **58**, 3242 (2004), https://doi.org/10.1016/j.matlet.2004.05.061

[52] K Sangwal, *Cryst. Res. Tech.* **44**, 1019 (2009), https://doi.org/10.1002/crat.200900385

[53] E M Onitsch, *Mikroskopie* **95**, 12 (1956)

[54] Y S Rammah, A S Abouhaswa and A H Salama, *J. Theoret. Appl. Phys.* **13**, 155 (2019), https://doi.org/10.1007/s40094-019-0331-6